Supporting information

Black Phosphorus@$Ti_3C_2T_x$ MXene Composites with Engineered Chemical Bonds for Commercial-Level Capacitive Energy Storage

Zhenghui Pan,[†] Lixing Kang,[‡] Tan Li,[§] Moaz Waqar,[†] Jie Yang,[&,*] Qilin Gu,[†] Ximeng Liu,[†] Zongkui Kou,[†] Zhao Wang,[†] Lirong Zheng,[#,*] John Wang[†,*]

[†]Department of Materials Science and Engineering, National University of Singapore, 117574 Singapore, Singapore

[‡]Division of Advanced Materials, Suzhou Institute of Nano-Tech and Nano-Bionics, Chinese Academy of Sciences, 215123 Suzhou, P. R. China

[§]College of Environment and Energy, South China University of Technology, 510000 Guangzhou, P. R. China

[&]Department of Chemical and Biomolecular Engineering, National University of Singapore, 4 Engineering Drive 4, Singapore 117585, Singapore.

[#]Beijing Synchrotron Radiation Facility Institute of High Energy Physics, Chinese Academy of Sciences, 100049 Beijing, P. R. China

[*]Corresponding Author: cheyjie@nus.edu.sg; zhenglr@ihep.ac.cn; msewangj@nus.edu.sg

Characterizations

The resulting samples were characterized using SEM (Zeiss, 5.0–20.0 kV), XRD (AXIS Ultra) and XPS (Bruker D8 diffractometer). The Raman spectroscopy was performed with the LabRAM HR Evolution Raman microscopes (HORIBA), and an Argon laser (λ = 514 nm, National Laser Model 800AL) was used as the excitation line. The N_2 adsorption-desorption isotherms were measured by a Micromeritics ASAP 2020 Brunauer-Emmett-Teller (BET) analyzer. The STEM, STEM-EDS and EELS studies were conducted using a JEOL ARM200F atomic resolution analytical electron microscope equipped with a cold field-emission gun and a new ASCOR 5th order aberration corrector, an Oxford X-max 100TLE solid state detector and a Gatan Quantum ER spectrometer. The X-ray absorption find structure spectra (Ti K-edge) were collected at 1W1B station in Beijing Synchrotron Radiation Facility (BSRF). The storage rings of BSRF were operated at 2.5 GeV with a maximum current of 250 mA. Using Si (111) double-crystal monochromator, the data collection was carried out in transmission mode using ionization chamber. All spectra were collected in ambient conditions.

Electrochemical characterization and calculations

All the SCs were characterized by an electrochemical workstation (Solartron 1470E) at room temperature. The CV and GCD measurements were conducted at room temperature to evaluate the electrochemical performance of SCs. The $C_{vol\text{-}electrode}$ of MXene and BP@MXene film electrodes were calculated by their CV curves on the following equation: $C_{vol-electrode} = \frac{1}{\Delta V s}\int_0^{\Delta V} j dV$, where j is the discharging current density (A cm^{-3}), $\int_0^{\Delta V} j dV$ is the integrated area of CV curve, ΔV is the potential window (V), and s is the scan rate (V s^{-1}). The $C_{vol\text{-}electrode}$ of MXene and BP@MXene film electrodes were calculated by their GCD curves on the following equation: $C_{vol-electrode} = -\frac{I\,\Delta t}{V\Delta V}$, where I is the discharging current (A), $\Delta V/\Delta t$ is the slope after drop at the beginning of each discharging curve, V is the geometrical volume of film electrodes. The volumetric energy density

against two electrodes ($E_{vol\text{-}electrode}$) in device was calculated using the following formula: $E_{vol\text{-}electrode} = C_{vol\text{-}electrode}U^2/8$, where U is the operating voltage. The volumetric energy density against the entire SC stack ($E_{vol\text{-}stack}$) was obtained based on the following formula: $E_{vol\text{-}stack} = E_{vol\text{-}electrode} \times f_{electrode}$, where $f_{electrode}$ is volume fraction of the electrode materials. The entire device stack includes two electrodes with electrolytes, two current collectors (Pt foils), one separator and parafilm packaging. The thickness and areal mass of one membrane separator with electrolyte are ~25 μm and ~ 3 mg cm^{-2}; the thickness and areal mass of one Pt current collector are ~20 μm and ~ 5.8 mg cm^{-2}; the thickness and areal mass of total wrapped parafilm package are ~100 μm and ~ 15 mg cm^{-2}; the thickness and areal mass of one thick electrode (15 mg cm^{-2} per film electrode) with electrolyte are ~225 μm and ~ 25 mg cm^{-2}. The $E_{vol\text{-}stack}$ were normalized by the total volume of the entire device with only consideration of electrode area, which is similar to the approach used in recent reports.[1,2] The various power densities of the device (P) were calculated from the following formula: $P = E/\Delta t$, where Δt is the discharge time.

Computational details

In this paper, the DMol3 module based on DFT using a numerical radial function was employed to view EMIM$^+$/TFSI$^-$ ions performance of MXene and BP@MXene capacitive energy storage.[3] The generalized gradient approximation (GGA) with Perdew–Burke–Ernzerhof (PBE) function exchange–correlation potential was employed for the geometry optimization.[4] The basis set adopted the double numerical basis plus polarization function (DNP).[5] The special *k*-point sampling scheme of Monkhorst-Pack was used for approximating the Brillouin zone integrations,[6,7] and 1 × 2 × 1 *k*-point grids were used. The spin-unrestricted and auto multiplicity state were also employed to calculate the total electron densities. Geometrical optimization was made, and convergence was assumed when the convergence tolerance of energy, maximum force and maximum displacement were less than 1.0 × 10^{-5} Ha, 0.002 Ha/Å and 0.005 Å, respectively. For achieving high quality

results, the real space global orbital cutoff radius was set as 5.2 Å and the smearing of orbital occupancy was 0.005 Ha.

Models for $EMIM^+/TFSI^-$ ions adsorbed on activation sites constructed to confirm the most stable adsorption models. After geometric optimization, the adsorption energies (E_G) of these molecules were calculated through the following equation:

$$E_G = E_{*A} - (E_* + E_A)$$

Where, E_{*A} and E_* are the energies of MXene or BP@MXene with and without adsorption molecules, respectively. E_A is the energy of a free molecule of the adsorption molecule. From this definition, a negative value of E_G indicates that the formation process is exothermic, and a more negative value corresponds to a more readily and preferred generation scenario.

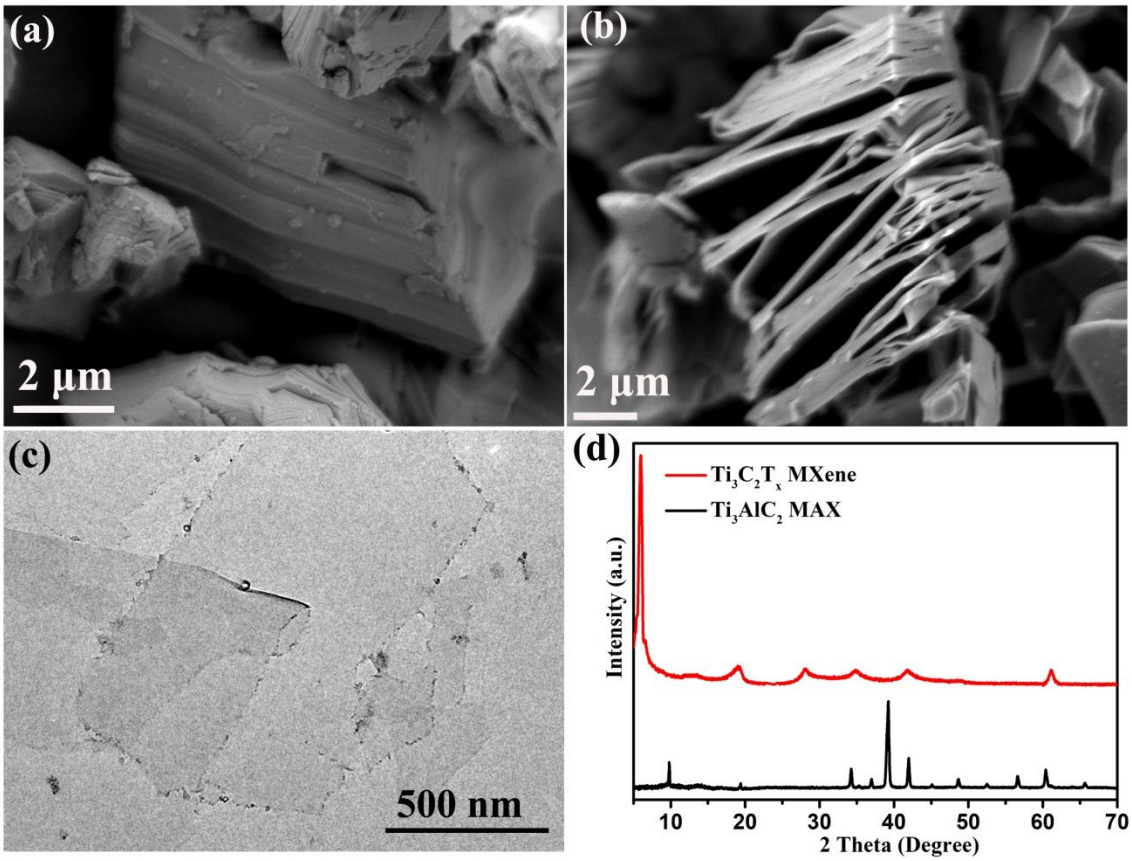

Figure S1. SEM images of (a) Ti_3AlC_2 MAX and (b) etched multilayered $Ti_3C_2T_x$ MXene. (c) Low-magnification TEM image of $Ti_3C_2T_x$ MXene. (d) XRD patterns of Ti_3AlC_2 MAX and $Ti_3C_2T_x$ MXene.

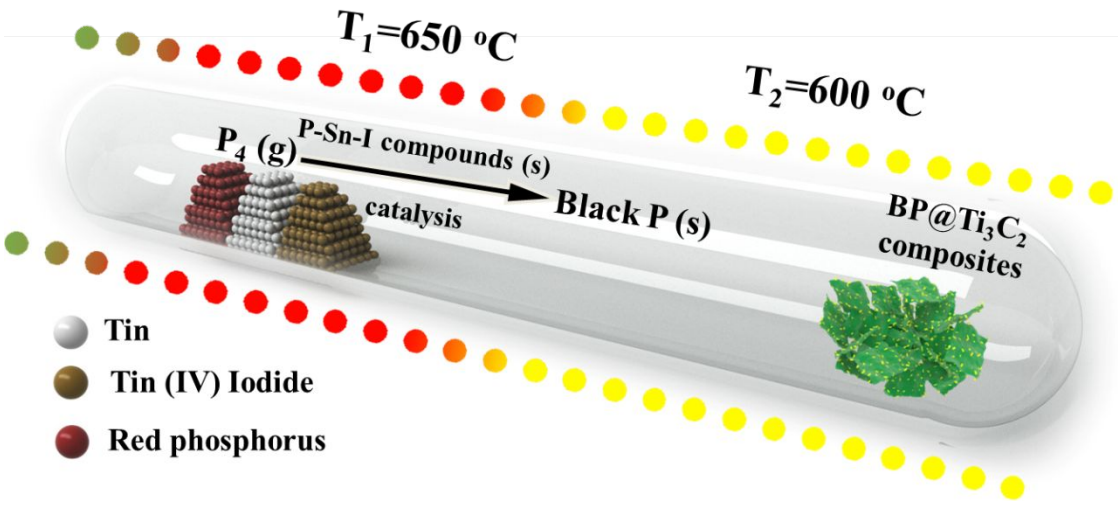

Figure S2. Schematic illustration of synthesizing BP@MXene composites with strong Ti-O-P bonds *via in situ* reaction at high temperature.

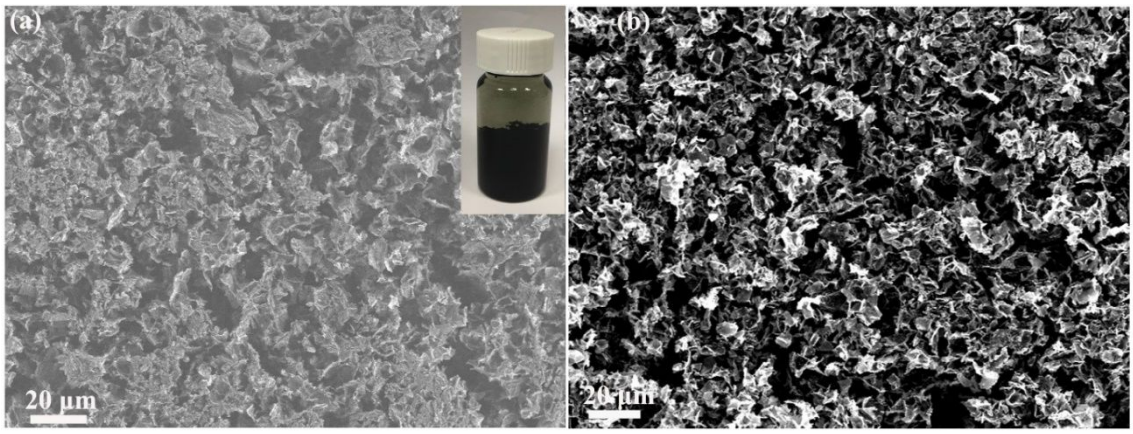

Figure S3. (a) SEM images of (a) the alkali-induced 3D crinkled $Ti_3C_2(OH)_x$ flakes and (b) the heterostructured BP@MXene composites. The inset in Figure (a) shows a free-standing hydrogel formed by $Ti_3C_2(OH)_x$ flakes.

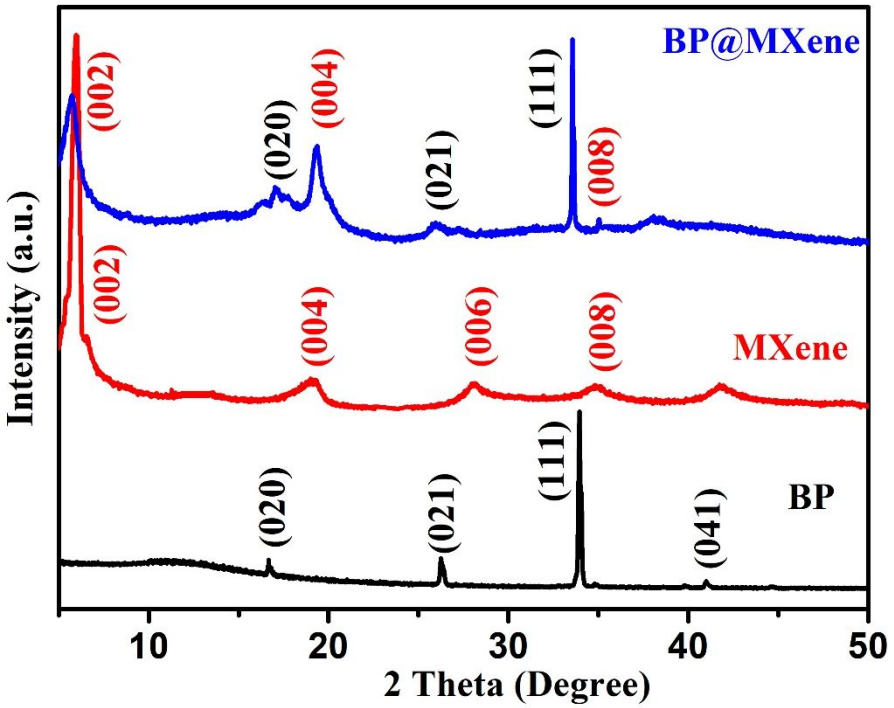

Figure S4. XRD patterns of BP, MXene and BP@MXene composite.

(a)

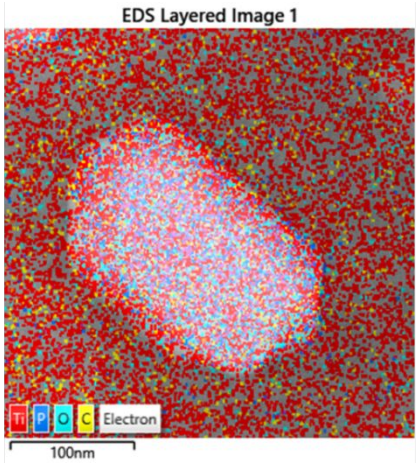

(b)

Element	wt%	at%
Ti	67.39	41.81
P	10.58	10.14
C	11.6	28.68
O	10.43	19.36

Figure S5. STEM-HAADF image (a) and the corresponding EDS results (b) of BP@MXene composite.

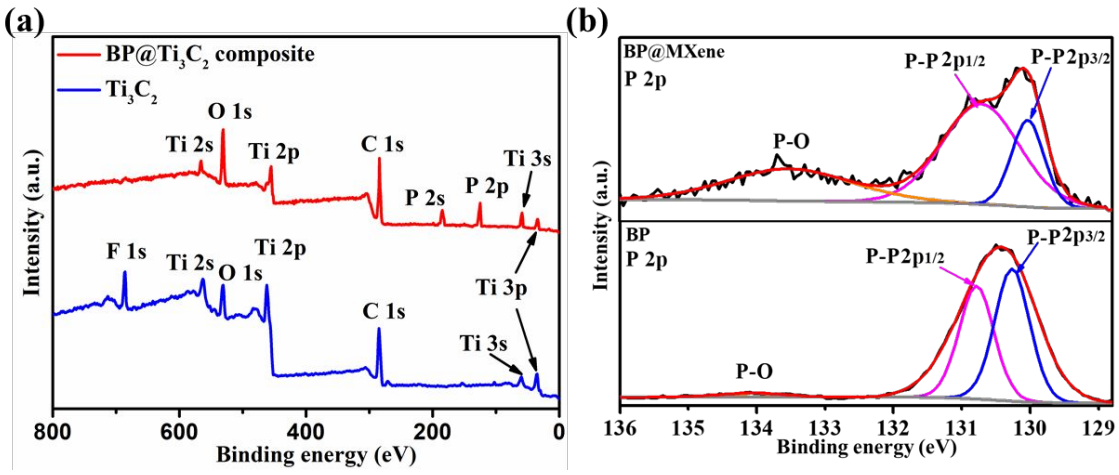

Figure S6. (a) XPS survey scans of MXene and BP@MXene composite. (b) High-resolution XPS spectra of P 2p of the BP@MXene composite and BP.

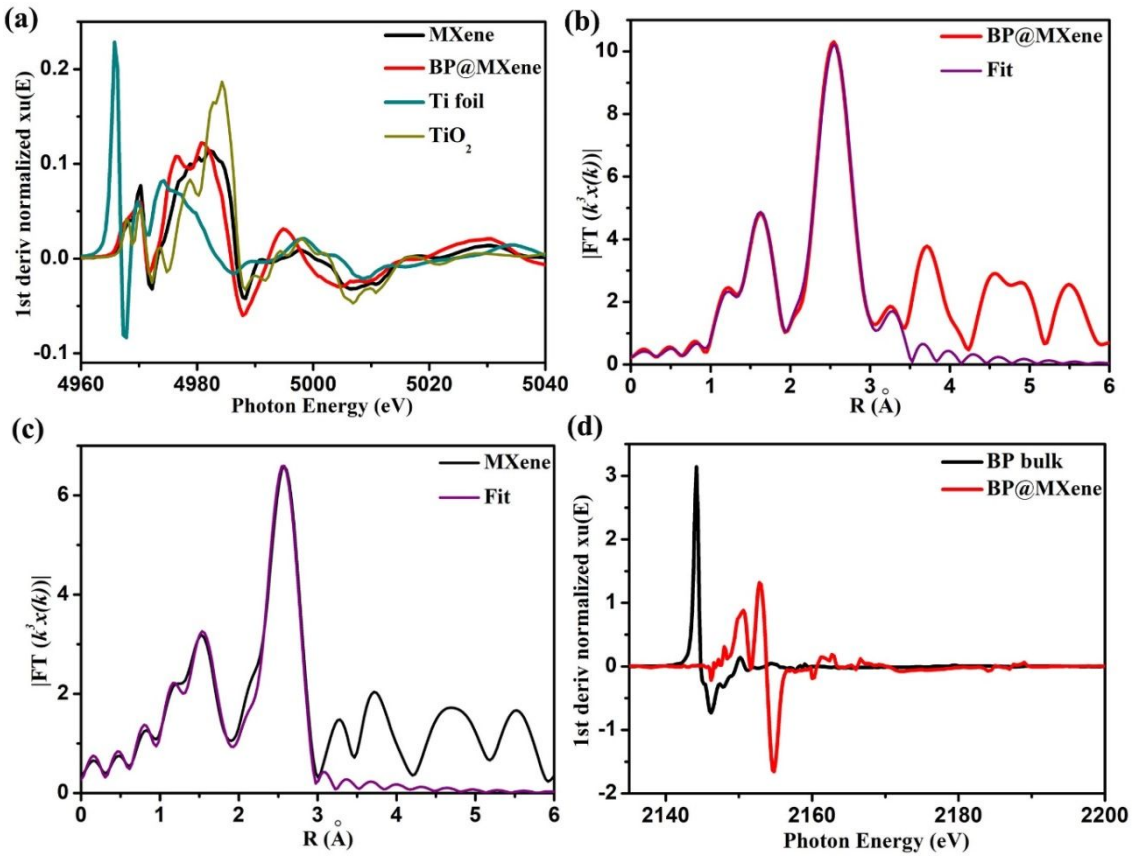

Figure S7. (a) The corresponding first derivatives of BP@MXene composites, MXene, Ti foil and TiO_2 at Ti K-edge XANES spectra. The corresponding EXAFS *R* space fitting curves of (b) BP@MXene composites and (c) MXene. (d) The corresponding first derivatives of BP@MXene composites and BP bulk at P K-edge XANES spectra.

Table S1. EXAFS fitting parameters at the Ti K-edge for various samples.

Sample	Shell	*N*	*R*(Å)	σ^2 (Å^2 × 10^{-3})	ΔE_0 (eV)	*R* factor (%)
BP@MXene	Ti-O(C)	5.4	2.08	12.0	0.9	0.4
	Ti-Ti	6.9	3.02	7.3	7.9	
	Ti-Ti	1.4	3.42	6.5	2.7	
MXene	Ti-O(C)	3.4	2.06	7.0	3.4	0.6
	Ti-Ti	6.0	2.99	6.9	8.0	
	Ti-Ti	1.4	3.48	6.5	2.7	

[a]*N*: coordination numbers; [b]*R*: bond distance; [c]σ^2: Debye-Waller factors; [d]ΔE_0: the inner potential correction. *R* factor: goodness of fit. *S*02 for Ti-N/Ti-Ti were set as 0.85/0.9, which were obtained from the experimental EXAFS fit by fixing CN as the known crystallographic value and was fixed to all the samples.[8-10]

Notes: Error bounds (accuracies) that characterize the structural parameters obtained by EXAFS spectroscopy were estimated as N ± 20%、σ^2 ± 20%; R ± 0.03 Å.

The acquired EXAFS data was processed according to the standard procedures using the ATHENA module implemented in the IFEFFIT software packages. The k^3-weighted EXAFS spectra were obtained by subtracting the post-edge background from the overall absorption and then normalizing with respect to the edge-jump step. Subsequently, k^3-weighted χ(k) data of Ti-K-edge were Fourier transformed to real (R) space using a hanning windows (dk = 1.0 Å^{-1}) to separate the EXAFS contributions from different coordination shells. To obtain the quantitative structural

parameters around central atoms, least-squares curve parameter fitting was performed using the ARTEMIS module of IFEFFIT software packages.

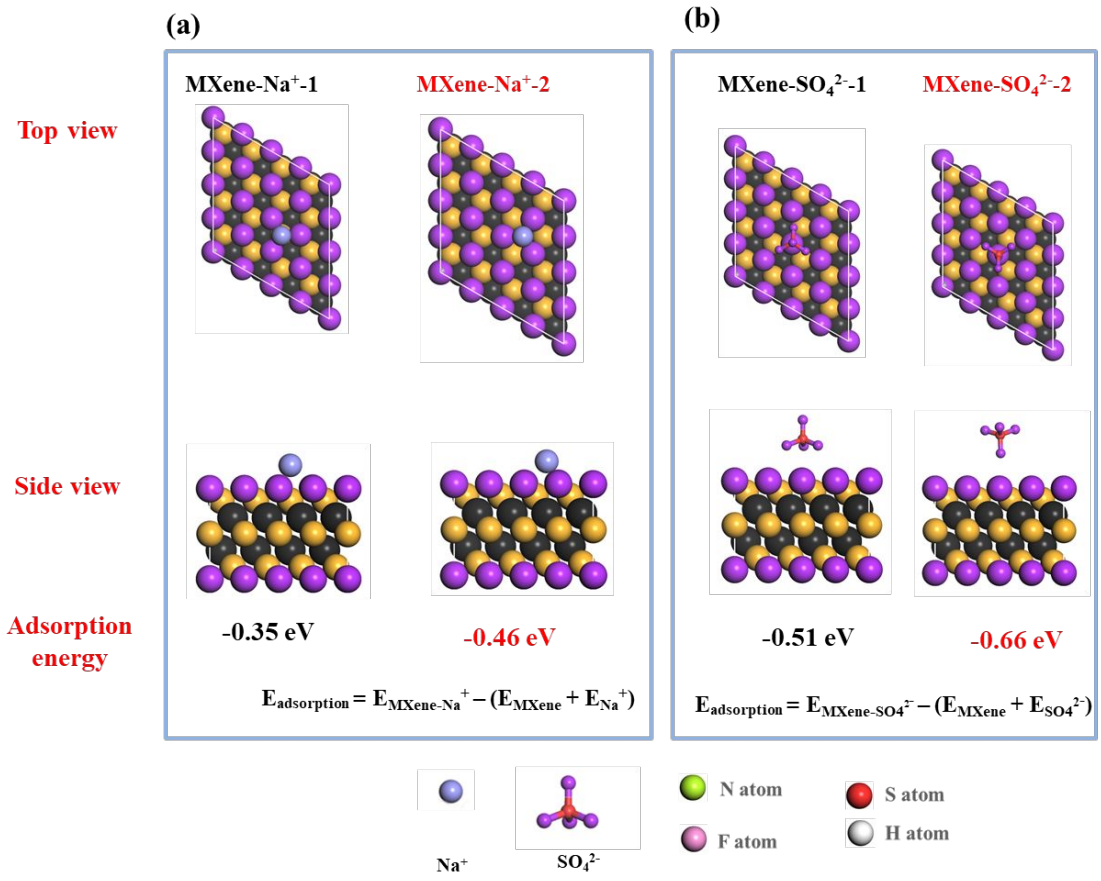

Figure S8. Top and side views of the slab models used to describe the (a) Na^+ ion and (b) SO_4^{2-} ion adsorbed on MXene, respectively. Atoms in yellow, black, purple and blue represent Ti, C, O and P, respectively.

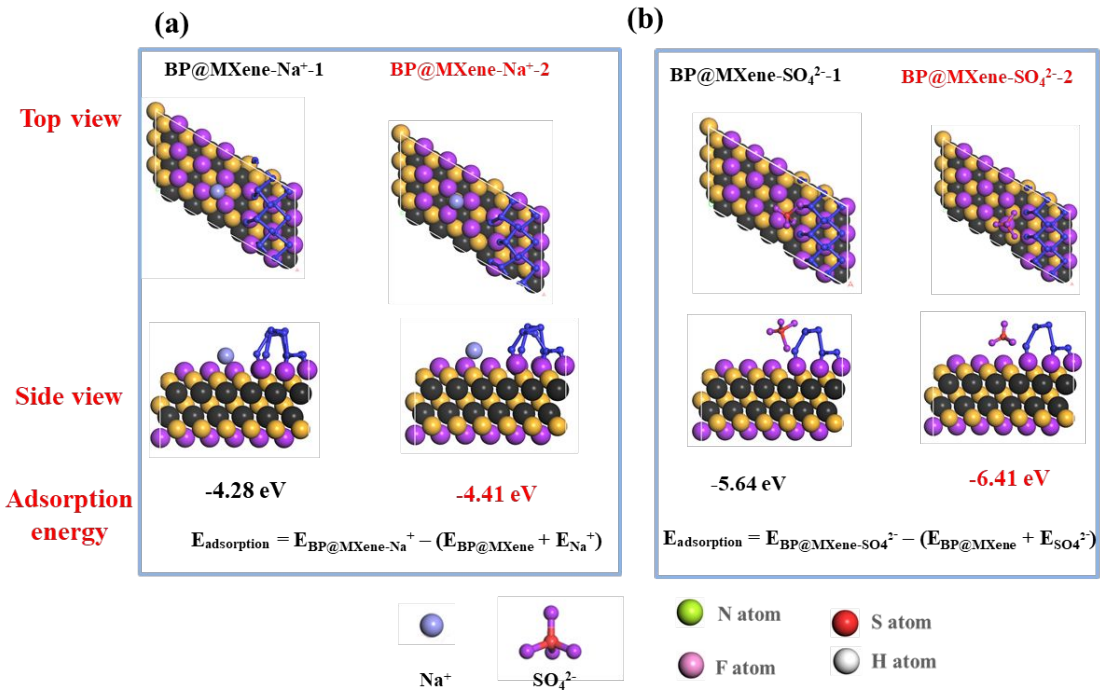

Figure S9. Top and side views of the slab models used to describe the (a) Na^+ ion and (b) SO_4^{2-} ion adsorbed on BP@MXene, respectively. Atoms in yellow, black, purple and blue represent Ti, C, O and P, respectively.

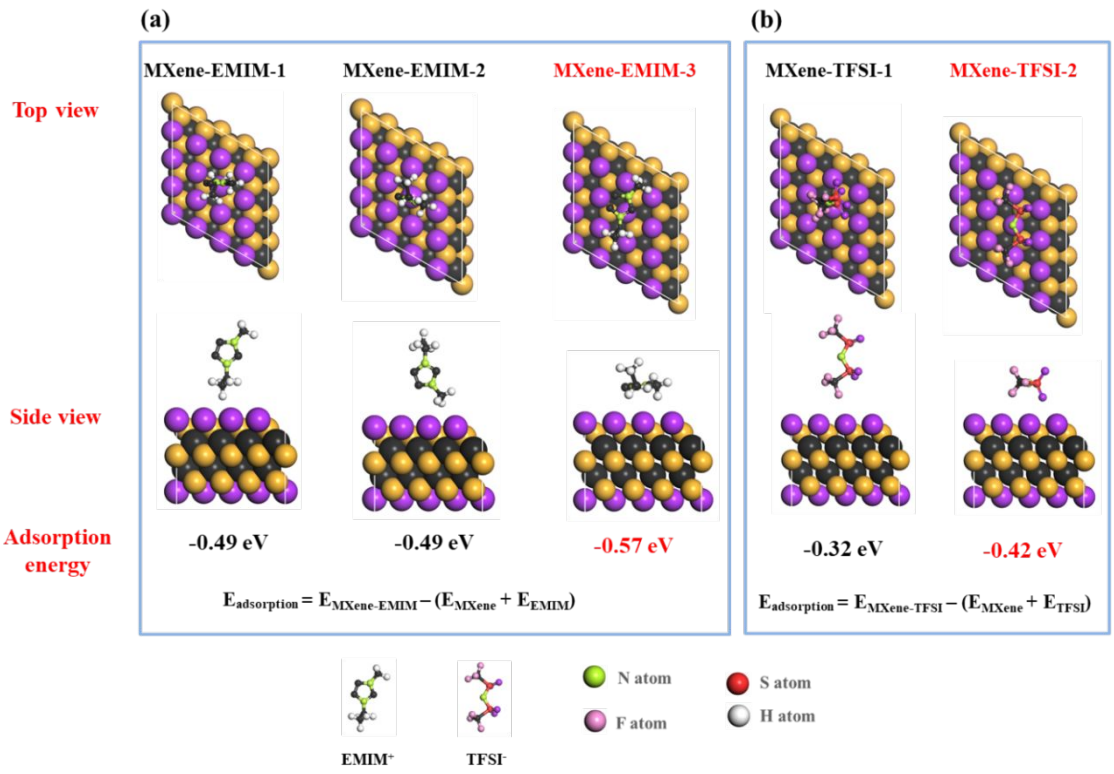

Figure S10. Top and side views of the slab models used to describe the (a) $EMIM^+$ ion and (b) $TFSI^-$ ion adsorbed on MXene, respectively. Atoms in yellow, black, purple and blue represent Ti, C, O and P, respectively.

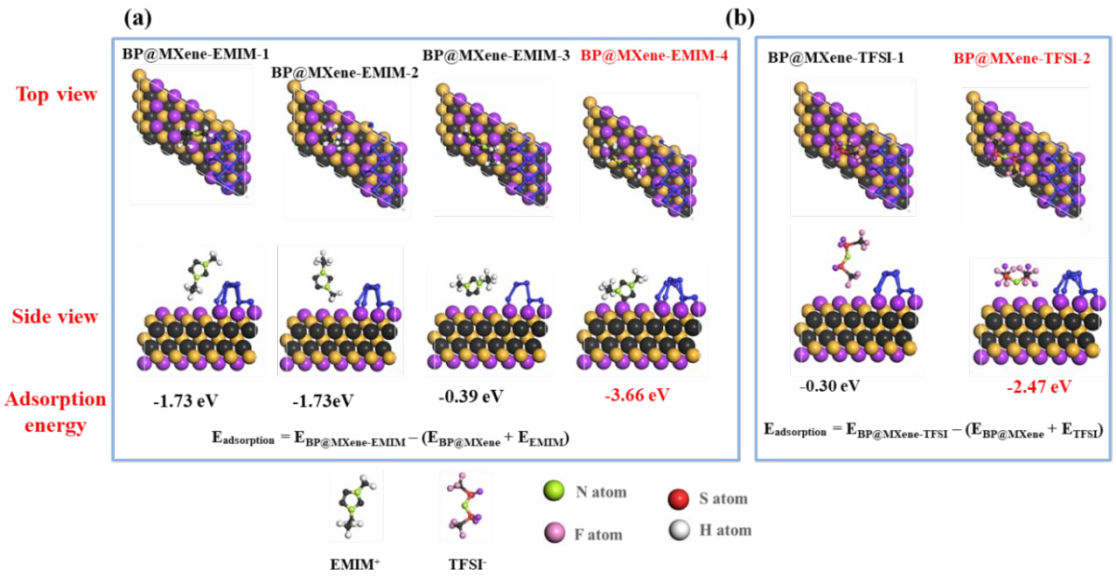

Figure S11. Top and side views of the slab models used to describe the (a) $EMIM^+$ ion and (b) $TFSI^-$ ion adsorbed on BP@MXene composite, respectively. Atoms in yellow, black, purple and blue represent Ti, C, O and P, respectively.

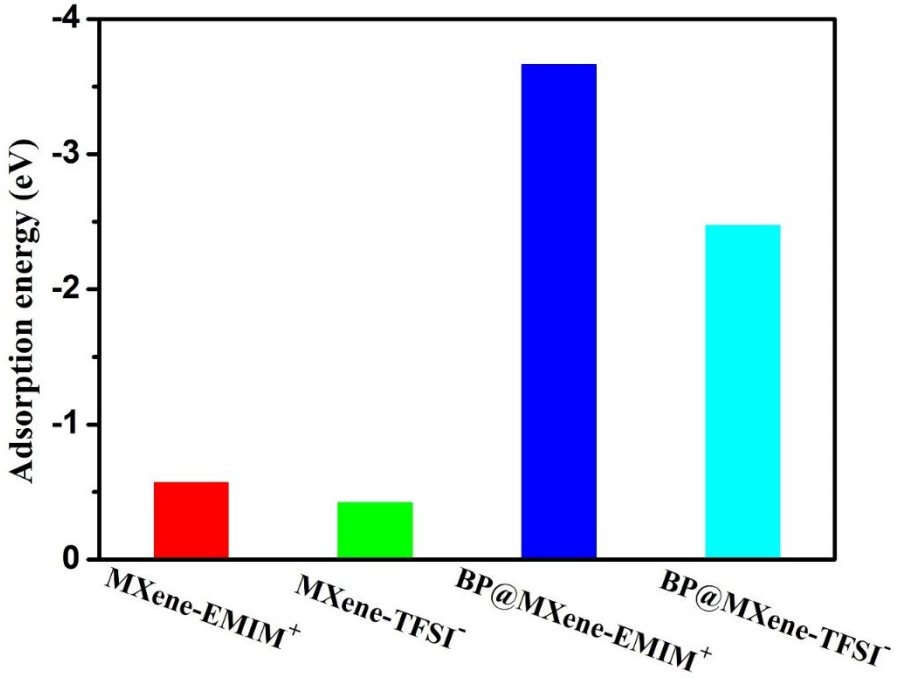

Figure S12. The calculated binding energies of the most stable $EMIM^+$ and $TFSI^-$ adsorption sites on MXene and BP@MXene.

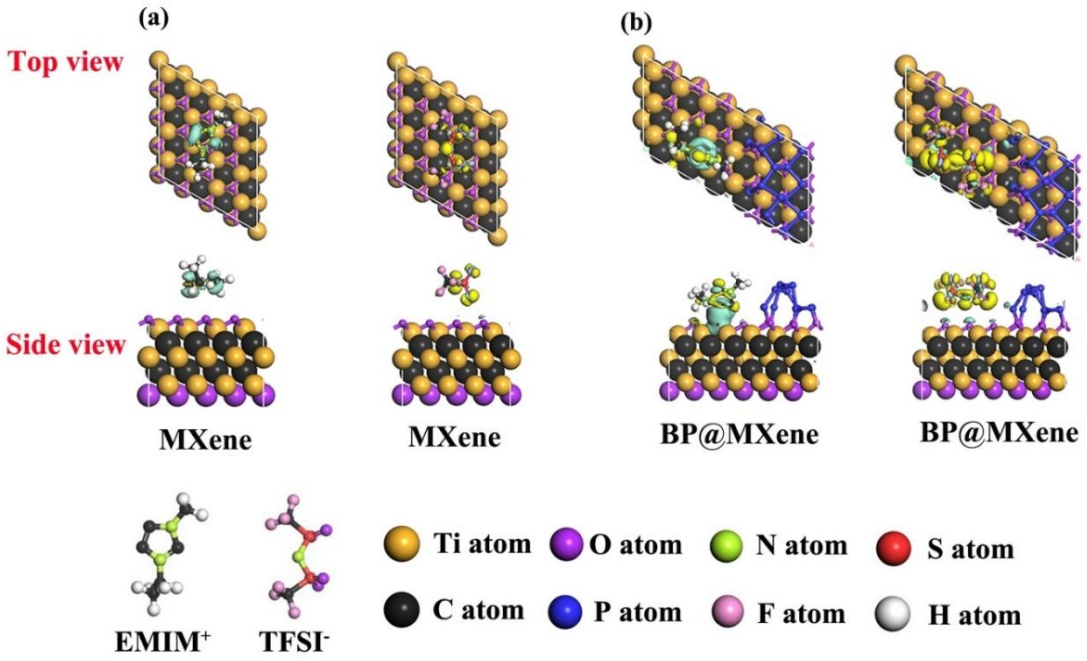

Figure S13. (a, b) Calculated charge density distribution differences between MXene and BP@MXene adsorbed with $EMIM^+$ and $TFSI^-$ ions.

Table S2. The adsorption energies for Na^+ ion and SO_4^{2-} ion adsorbed on MXene and BP@MXene composite, respectively.

Sample	Adsorption type	Adsorption energy (eV)
MXene	MXene-Na^+-1	-0.35
	MXene-Na^+-2	**-0.46**
	MXene-SO_4^{2-}-1	-0.51
	MXene-SO_4^{2-}-2	**-0.66**
BP@MXene	BP@MXene-Na^+-1	-4.28
	BP@MXene-Na^+-2	**-4.41**
	BP@MXene-SO_4^{2-}-1	-5.64
	BP@MXene-SO_4^{2-}-2	**-6.41**

Table S3. The adsorption energies for $EMIM^+$ ion and $TFSI^-$ ion adsorbed on MXene and BP@MXene composite, respectively.

Sample	Adsorption type	Adsorption energy (eV)
MXene	MXene-$EMIM^+$-1	-0.49
	MXene-$EMIM^+$-2	-0.49
	MXene-$EMIM^+$-3	**-0.57**
	MXene-$TFSI^-$-1	-0.23
	MXene-$TFSI^-$-2	**-0.42**
BP@MXene	BP@MXene-$EMIM^+$-1	-1.73
	BP@MXene-$EMIM^+$-2	-1.73
	BP@MXene-$EMIM^+$-3	-0.39
	BP@MXene-$EMIM^+$-4	**-3.66**
	BP@MXene-$TFSI^-$-1	-0.3
	BP@MXene-$TFSI^-$-2	**-2.47**

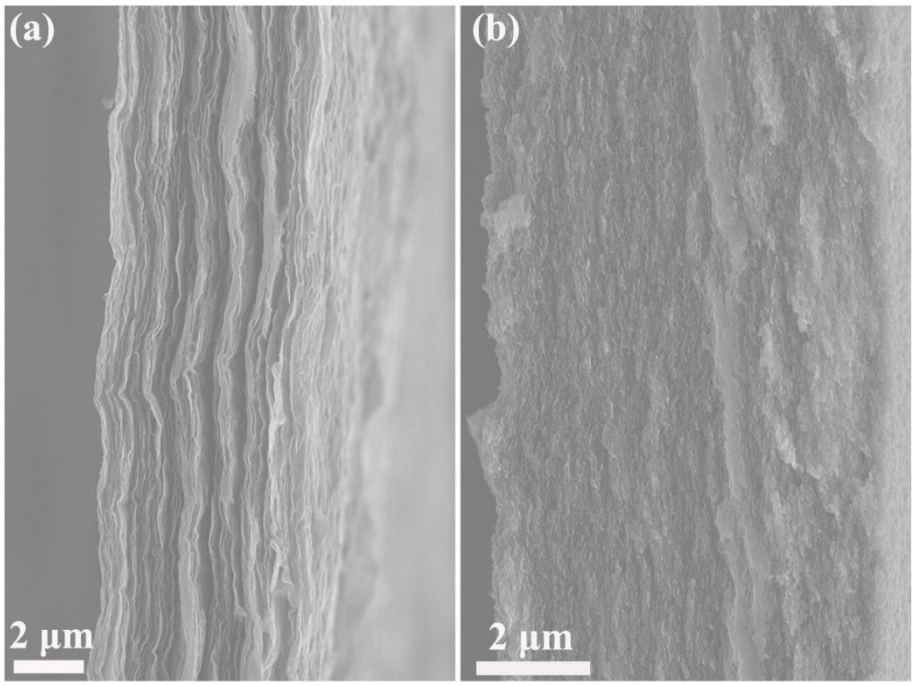

Figure S14. The cross-sectional SEM images of lamellar structured BP@MXene film (a) and MXene film (b).

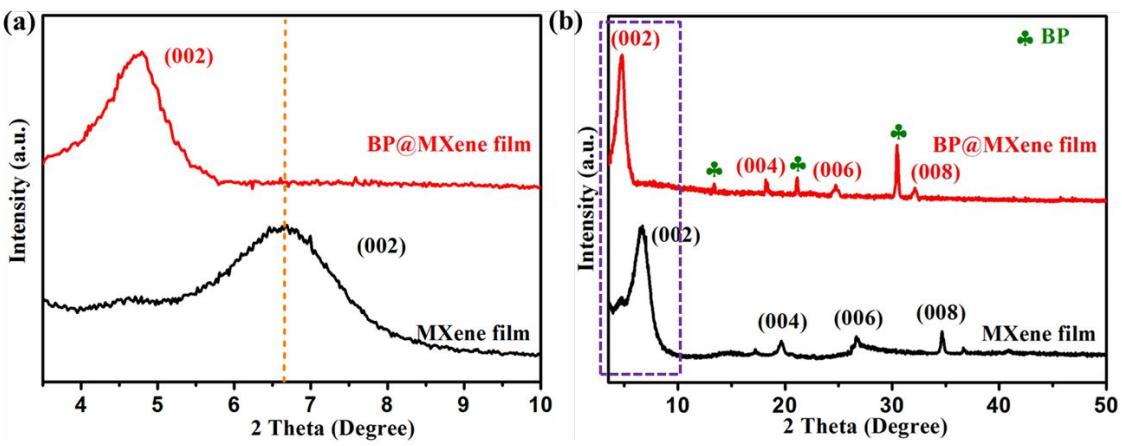

Figure S15. XRD patterns of MXene and BP@MXene films.

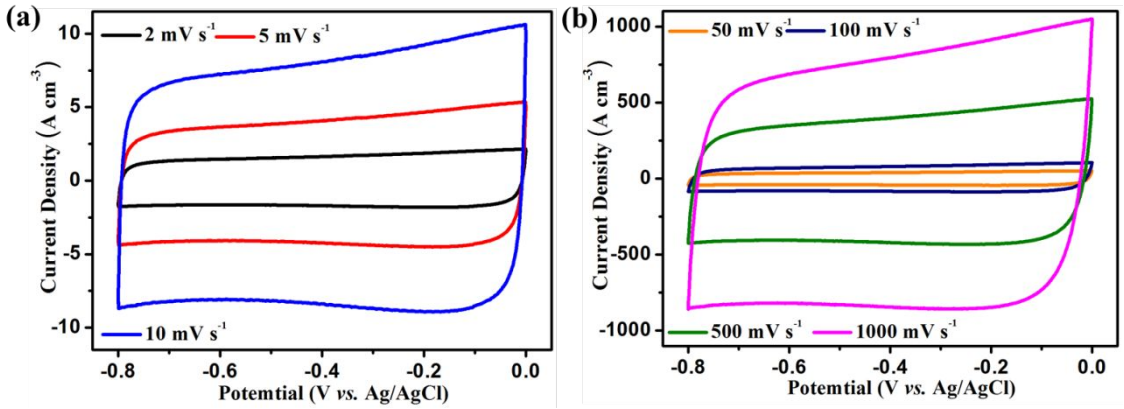

Figure S16. CV curves of the BP@MXene film electrode in three-electrode electrochemical cell at various scan rates ranging from 2.0 to 1000 mV s^{-1} in 1.0 M Na_2SO_4 electrolyte.

In 1.0 M Na_2SO_4 electrolyte at neutral pH, the free-standing BP@MXene film was evaluated as a working electrode in a three-electrode electrochemical cell (Ag/AgCl as the reference electrode; Pt foil as counter electrode), which was saturated by N_2 before testing. As show in Figure S16, the stable operation potential window of the BP@MXene film electrode can be observed between –0.8 and 0.0 V, which is consistent with the previously reported results of MXene-based electrodes texted in neutral electrolytes. Moreover, all CV curves from the scan rates of 2.0–1000 mV s^{-1} present nearly rectangular shapes, indicating the capacitive behaviour and the outstanding reversibility of the BP@MXene film electrode.

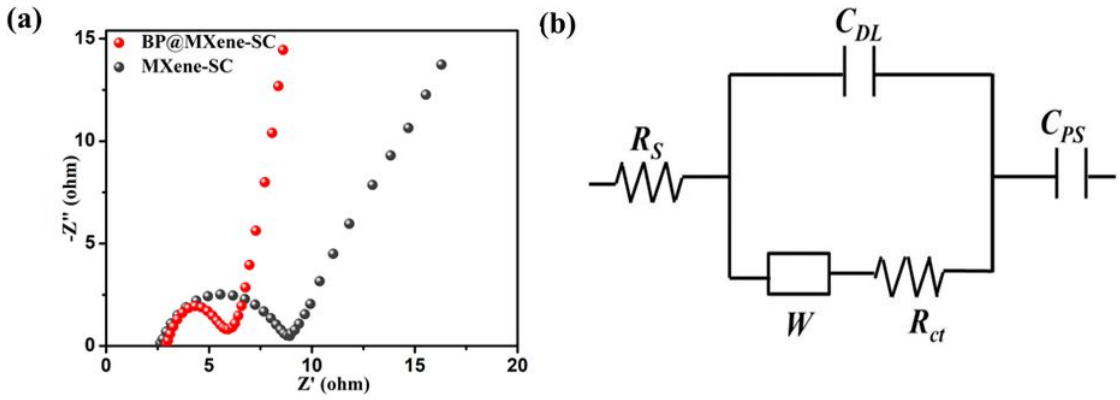

Figure S17. (a) EIS plots and (b) the corresponding equivalent circuit of MXene and BP@MXene-SCs in 1M Na_2SO_4 electrolyte.

As shown in Figure S17(b), the impedance data were analyzed by fitting with an equivalent circuit consisting of the series resistance (R_s), charge transfer resistance (R_{ct}), double layer capacitance (C_{DL}) and Warburg impedance (Z_W). At high frequency range, the value of the intercept at the real axis is used to estimate the R_S of the electrodes, which is the combination of the ionic resistance of the electrolyte and the resistance of the electrode material itself. The semicircle diameter in the plot corresponds to the R_{ct}, also called Faraday resistance, corresponding to the total resistance at the interface between the electrode and the electrolyte. In addition, R_{ESR} is the equivalent series resistance of the device, which was calculated *via* dividing the voltage drop (U_{drop}) at the beginning of the discharge by the applied constant current (I) using the formula: $R_{ESR} = U_{drop}/2I$. It should be noted that the R_{ESR} of an SC is related to both R_S and R_{CT} in the electrodes. Figure S17 (a) and Table S4 present the R_s values of the BP@MXene-SC and MXene-SC in 1.0 M Na_2SO_4 electrolyte are 2.94 Ω and 2.28 Ω, showing almost no variation in the total resistance between BP@MXene and MXene films. However, the R_{ct} of the SCs decreases from 5.35 Ω to 2.92 Ω after the introduction of BP nanoparticles onto the surface of MXene flakes, demonstrating that BP nanopartilces can not only serve as effective nanospacers to expand the nanofluidic channels of MXene multilayers in the compact film electrode, thereby accelerating electrolyte ion transportation,

but also effectively isolate the aggregation and face-to-face self-restacking of MXene flakes during film electrode fabrication processes. Furthermore, an R_{ESR} of 5.86 Ω and 7.63 Ω was obtained for the BP@MXene-SC and the MXene-SC respectively.

Table S4. Fitting results for EIS of the two SCs in 1.0 M Na_2SO_4 electrolyte.

Devices	R_s **(Ω)**	R_{ct} **(Ω)**	R_{ESR}	C_{DL}	Z_W
BP@MXene-SC	2.94	2.92	5.86	0.76321	0.68479
MXene-SC	2.28	5.35	7.63	0.78468	0.65347

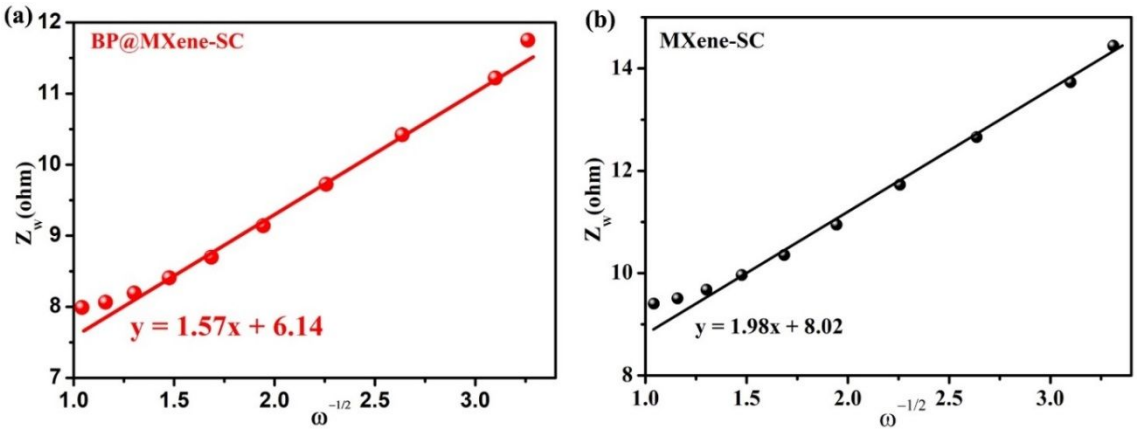

Figure S18. Linear relations between Z_w and $\omega^{-1/2}$ of (a) BP@MXene-SC and (b) MXene-SC in 1.0 M Na_2SO_4 electrolyte.

To understand the kinetics of electrolyte diffusion within BP@MXene film electrode, the depressed semicircle at medium frequencies presenting the ion-diffusion resistance was fitted *via* following equation,

$$Z_w = R_s + R_{ct} + \sigma\omega^{-1/2}$$

, where σ is the Warburg factor (the diffusion coefficient of Na^+ ions [D_{Na+}], which is inversely proportional to σ^{-2} [$D_{Na+} \propto 1/\sigma^2$]), and ω is the frequency.

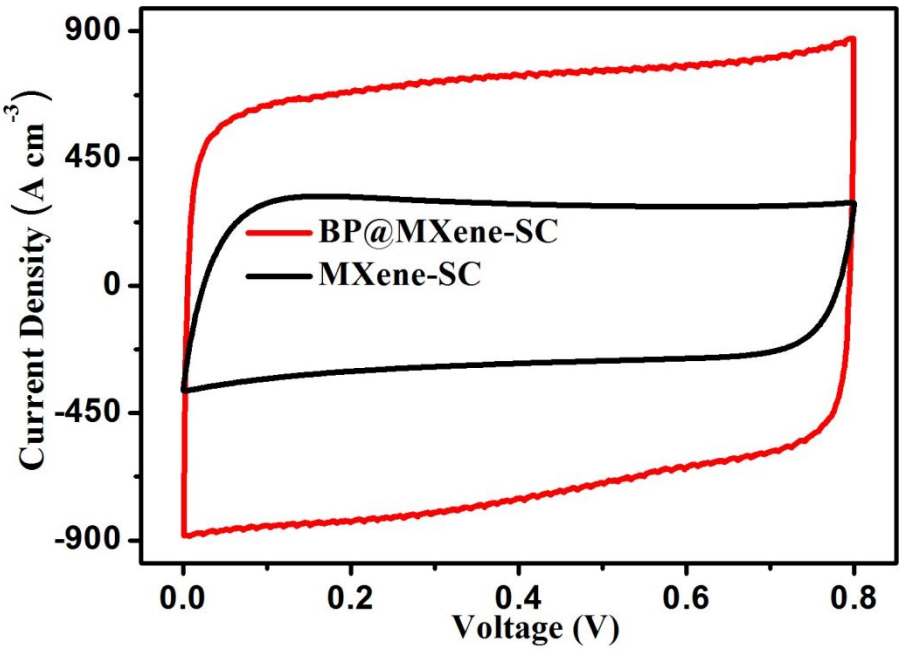

Figure S19. CV curves at a scan rate of 1000 mV s^{-1} of MXene and BP@MXene-SCs in 1.0 M Na_2SO_4 electrolyte.

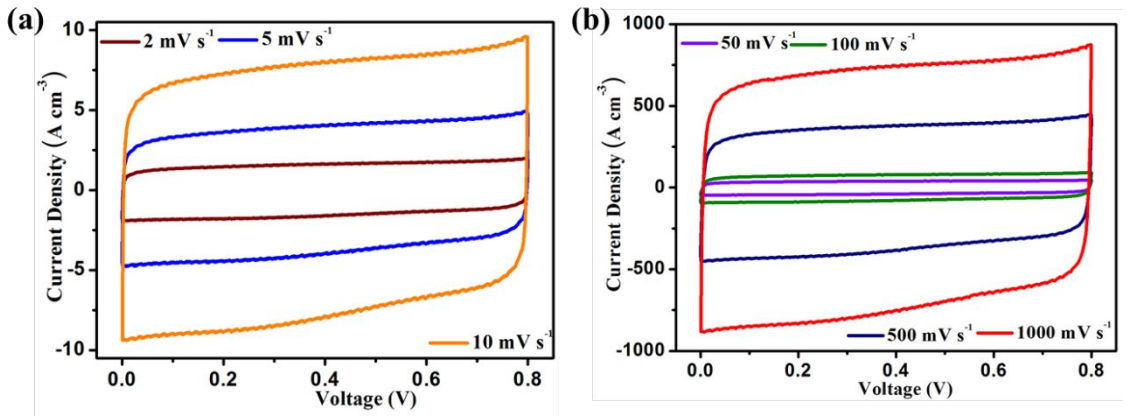

Figure S20. CV curves of BP@MXene-SC at various scan rates ranging from 2.0 to 1000 mV s^{-1} in 1.0 M Na_2SO_4 electrolyte.

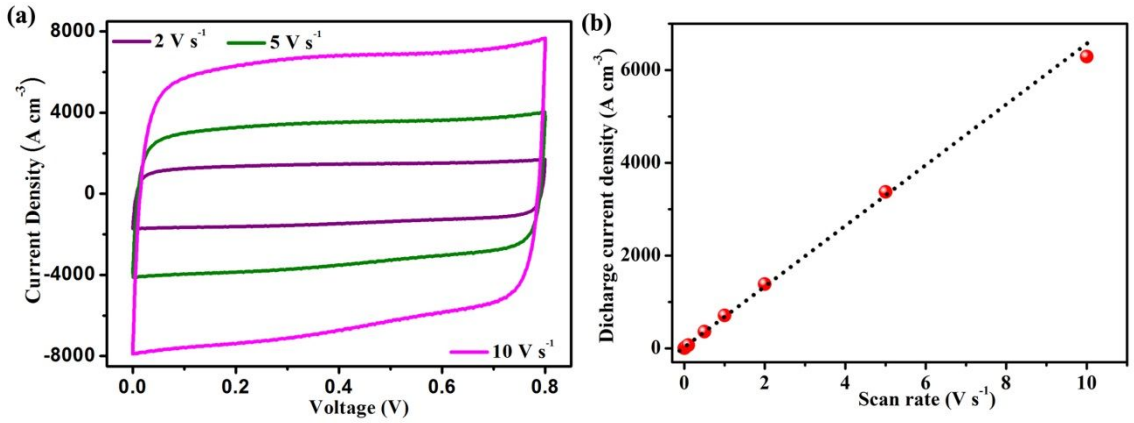

Figure S21. (a) CV curves of BP@MXene-SC at various scan rates ranging from 2.0 to 10 V s^{-1} in 1.0 M Na_2SO_4 electrolyte. (b) Plot of discharging currents *versus* scan rates for the BP@MXene-SC.

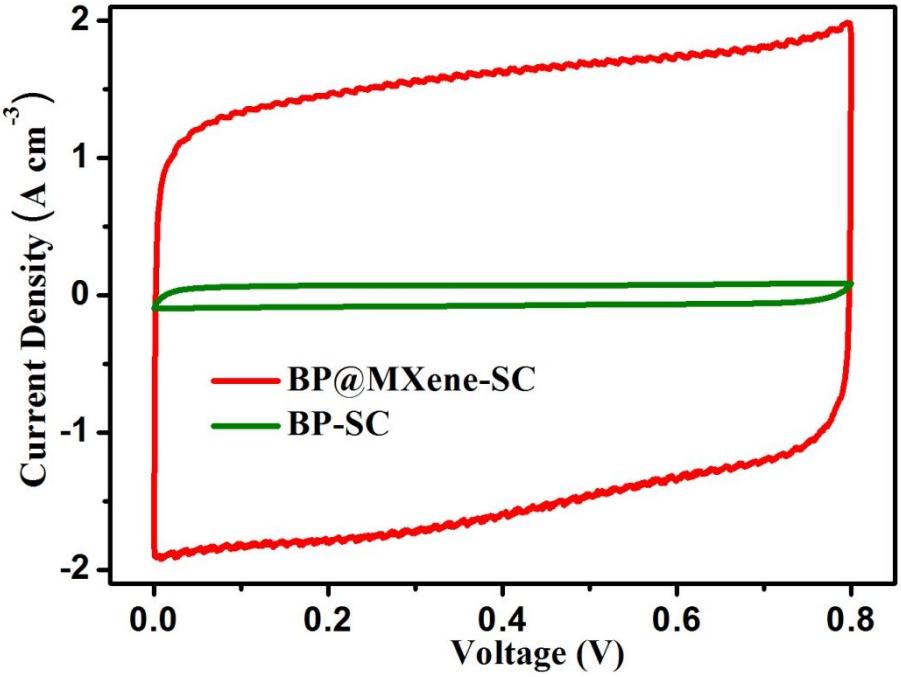

Figure S22. Comparisons of CV curves at a scan rate of 2.0 mV s^{-1} of BP and BP@MXene-SCs in 1.0 M Na_2SO_4 electrolyte.

Table S5. Comparison of electrochemical performance of BP@MXene film electrode with previously reported MXene-based electrodes in different electrolytes.

Electrode (–)	Electrolyte (–)	Maximal volumetric capacitance of electrode ($C_{vol\text{-}electrode}$, F cm^{-3})	Scan rate (mV s^{-1})	Capacitance retention (%)	Refs
Neutral Electrolytes					
BP@MXene	**1.0 M Na_2SO_4**	**781.6**	**2–1000**	**91.2%**	**This Work**
MXene		**452.3**	**2–1000**	**60.9%**	
d-Ti_3C_2	1.0 M Li_2SO_4	633	2–200	51.0%	[11]
MnO_x-Ti_3C_2	1.0 M Li_2SO_4	602	2–200	39.0%	[12]
$Ti_3C_2T_x$/SWCNT	1.0 M $MgSO_4$	390	2–200	71.8%	[13]
Acidic Electrolytes					
MXene/rGO	3.0 M H_2SO_4	1040	2–1,000	61.0%	[14]
PEDOT:PSS /$Mo_{1.33}C$	1.0 M H_2SO_4	949	2–1,000	33.3%	[15]
PANI@M-$Ti_3C_2T_x$	3.0 M H_2SO_4	1632	10–5,000	50.7%	[16]
$Ti_3C_2T_x$ hydrogel	3.0 M H_2SO_4	1500	2–1,000	53.3%	[17]
$Ti_3C_2T_x$ clay	1.0 M H_2SO_4	900	2–100	80.2%	[18]
MX-rHGO_3	3.0 M H_2SO_4	1445	2–500	69%	[19]
Mo_2CT_x	1.0 M H_2SO_4	900	2–100	64.3%	[20]
Na-V_2CT_x	3.0 M H_2SO_4	1315	5–1000	45.6%	[21]
Alkaline Electrolytes					
$RuO_2 \cdot xH_2O$ @MXene-AgNW	PVA/KOH gel electrolyte	864	1–2000	35.1%	[22]
d-Ti_3C_2/CNT	6.0 M KOH	393	5–100	80.0%	[23]
$Ti_3C_2T_x$/SWCNT	1.0 M KOH	314	2–100	65.3%	[24]

ZnO/Ti_3C_2	1.0 M KOH	200	2–100	75.0%	[25]
MXene Paper	1.0 M KOH	442	2–100	62.2%	[26]

Note | rGO–reduced graphene oxide; PEDOT:PSS–poly(3,4-ethylenedioxythiophene) polystyrene sulfonate; MX-$rHGO_3$-MXene-reduced holey graphene oxide; CNT–carbon nanotube; SWCNT–single wall carbon nanotube; d-Ti_3C_2 MXene–delaminated Ti_3C_2 MXene.

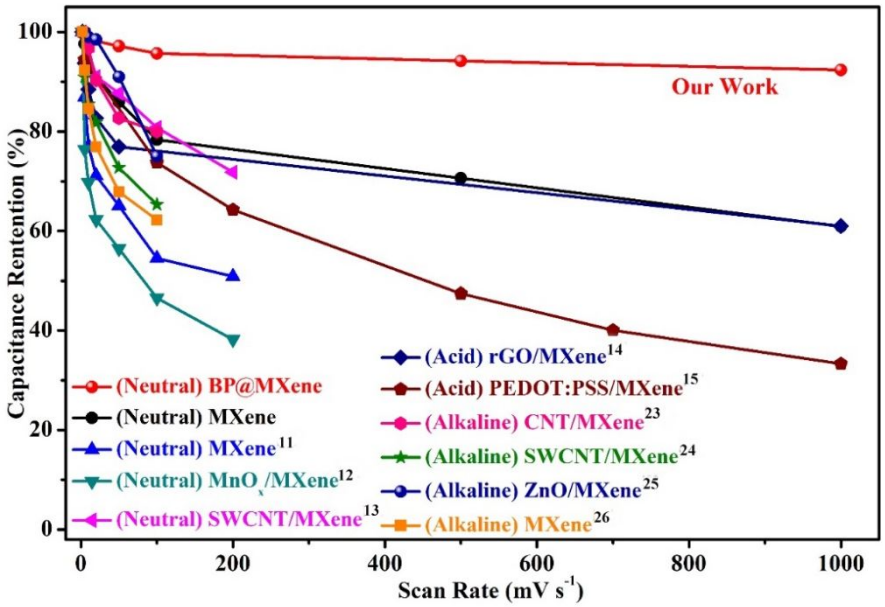

Figure S23. Comparison of rate performance of BP@MXene-SC with those of reported MXene-based electrodes.[11-15, 23-26]

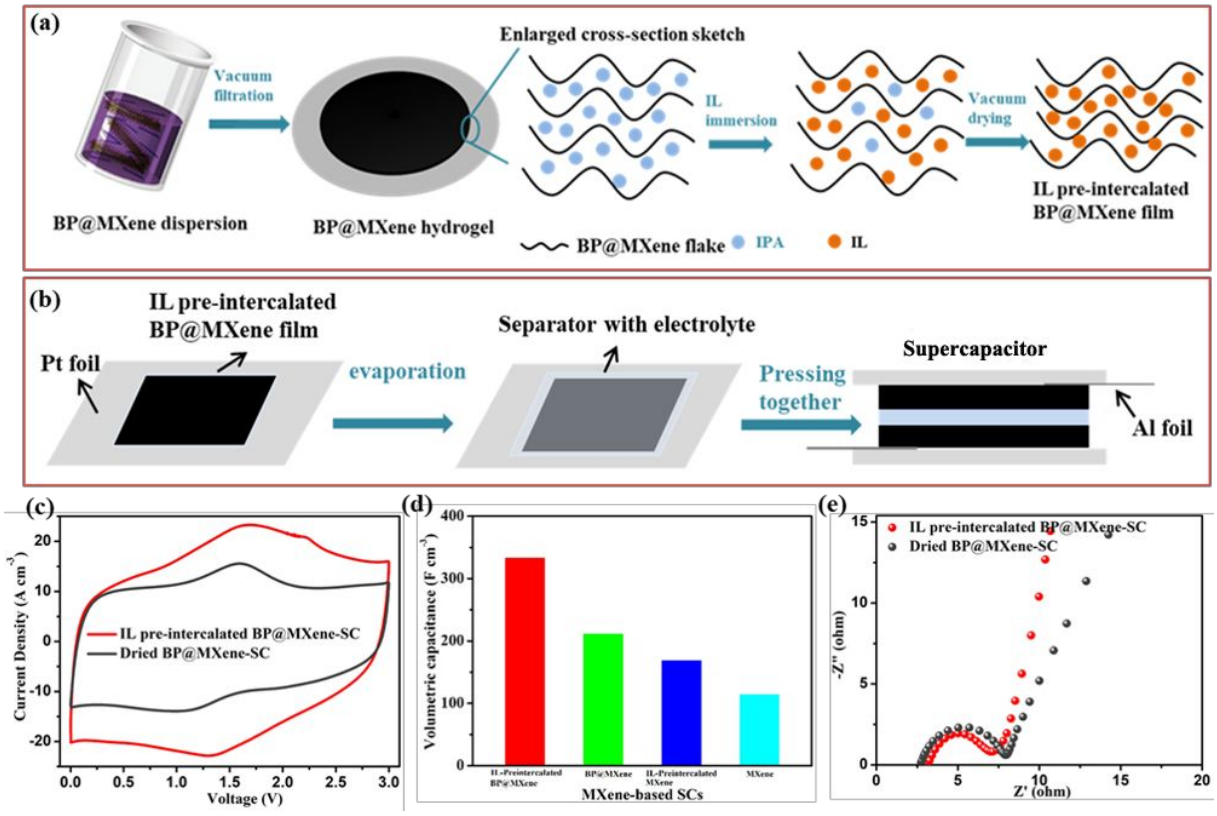

Figure S24. Schematic illustration of (a) preparing IL pre-intercalated BP@MXene film and (b) fabricating symmetric supercapacitor based on IL pre-intercalated BP@MXene film. Comparison of (c) CV curves tested at 50 mV s^{-1}, (d) volumetric capacitances and (d) EIS plots of IL pre-intercalated BP@MXene and MXene-SCs.

Indeed, various ionic liquids (ILs) have been recently employed for MXene-based SCs, which allow for the expansion of their maximum device voltage (up to ~3.0–3.5 V), but the insufficient accessibility to the large ions of ILs impedes the full utilization of the surface area thus leading to poor capacitance and rate capability. In this regard, we developed a reported strategy to obtain IL pre-intercalated BP@MXene compact film with a high ion-accessible surface area and low ion transport resistance (Figure S24a).[27] To investigate the importance of IL pre-intercalation into the BP@MXene film for the performance enhancement of SCs, we assembled two different kinds of SCs based on IL pre-intercalated BP@MXene film and dried BP@MXene film (drying at 120 °C for 24 h

under vacuum, Figure 24b-d), respectively, and the electrochemical performance of as-assembled SCs were tested in neat 1-ethyl-3-methylimidazolium bis(trifluoromethylsulfonyl)imide (EMIMTFSI) electrolyte with a working voltage of 3.0 V. Note that the EMIMTFSI IL is primarily chosen in our work because of its high viscosity and high specific conductivity. Figure S242(c) shows the CV curves of both two SCs at a scan rate of 50 mV s^{-1}, in which the IL pre-intercalated BP@MXene film delivers obviously higher integration area than dried BP@MXene, indicative of the improved C_{vol} of IL pre-intercalated BP@MXene-SC. As a result, the IL pre-intercalated BP@MXene film delivers a C_v of 332.6 F cm^{-3} (Figure 24d), which is 1.58 times higher than that of dried BP@MXene film (210.8 F cm^{-3}). It should be noted that the redox peaks in CV curves resulted from the insertion and extraction of $EMIM^+$ cations during charge and discharge processes. Furthermore, the electrochemical impedance spectrum (EIS) of IL pre-intercalated BP@MXene-SC presents a lower charge transfer resistance (R_{ct}) in the high-frequency region and a larger slope in the low-frequency region (Figure S24e), in comparison with that of dried BP@MXene-SC, reflecting a faster ion dynamics and more efficient electrolyte diffusion within the IL pre-intercalated BP@MXene film electrode. These above-mentioned results indicate that the pre-intercalation of the IL electrolyte into BP@MXene film with expanded interlayer spacing can intensively accommodate more available ions, providing a high ion-accessible surface area and low ion transport resistance, and thus dramatically increase the overall electrochemical performance of BP@MXene active materials.'

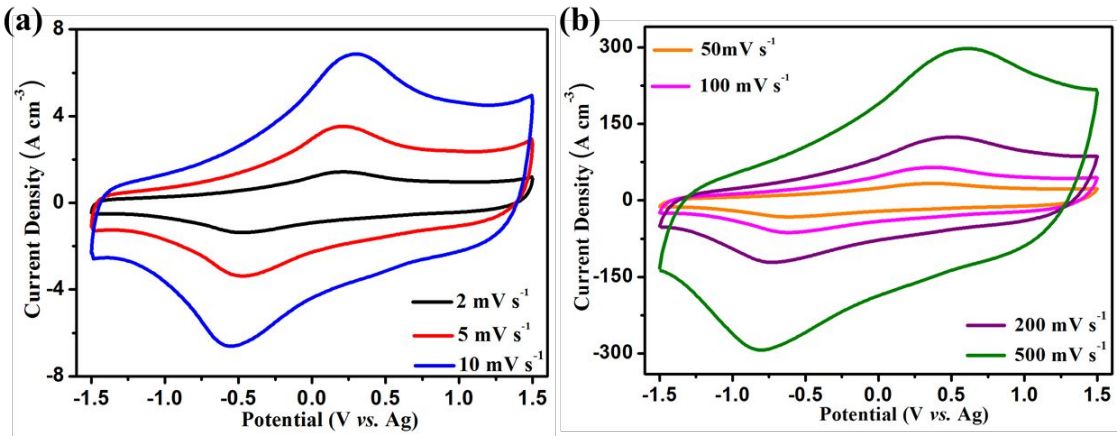

Figure S25. CV curves of the IL pre-intercalated BP@MXene film electrode in a three-electrode Swagelok cell at various scan rates ranging from 2.0 to 500 mV s^{-1} in neat EMIMTFSI IL electrolyte.

The IL pre-intercalated BP@MXene film was evaluated as the working electrode in a three-electrode Swagelok symmetric cell (an Ag wire as quasi-reference electrode and a commercial activated carbon as counter electrode) in neat EMIMTFSI IL electrolyte at room temperature. As shown in Figure S25, the symmetric CV shapes indicate a capacitive behavior within a potential window from –1.5 V to 1.5 V *vs.* Ag. The obvious redox peaks have resulted from the insertion and extraction of $EMIM^+$ cations and/or $TFSI^-$ anions under negative, and positive polarizations can be observed in all CV curves. Moreover, all CV curves from the scan rates of 2.0–500 mV s^{-1} maintain similar shapes with a slight shift in the anodic and cathodic peaks, demonstrating an excellent capacitive behavior.

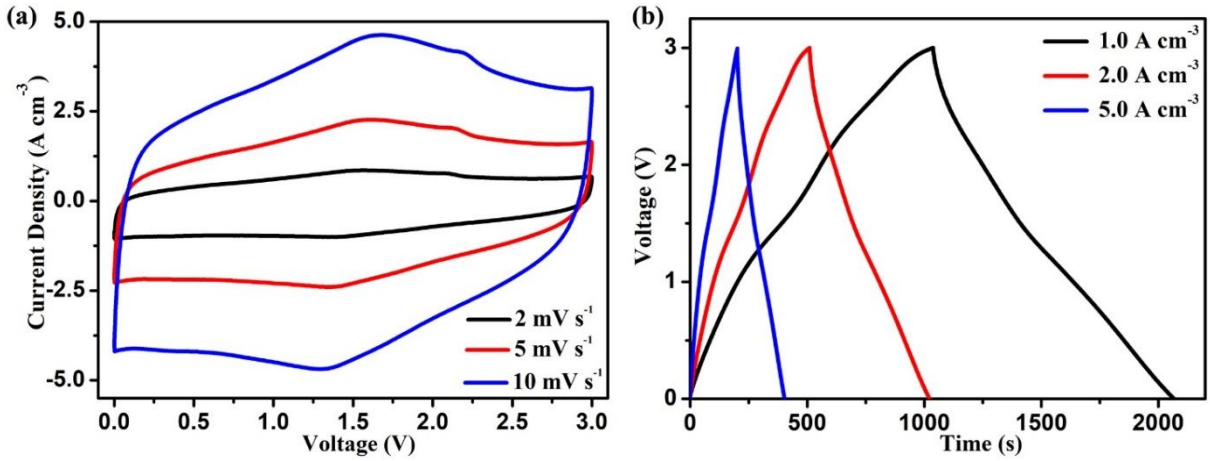

Figure S26. (a) CV curves under different scan rates. (e) GCD curves of as-assembled BP@MXene-SC in EMIMTFSI.

Table S6. Comparison of electrochemical performance of BP@MXene composite film electrode with other reported MXene and 2D material-based electrodes with IL and organic electrolyte.

Electrode (–)	Electrolyte (–)	Maximal volumetric capacitance of electrode ($C_{vol\text{-}electrode}$, F cm^{-3})	Current density or Scan rate (A cm^{-3} or mV s^{-1})	Capacitance retention (%)	Refs
MXene-based film electrodes					
BP@MXene	**Neat EMIMTFSI** (0-3.0 V) **Two-electrode system**	**342.3 (1.0 A cm^{-3})**	**1.0-100 (A cm^{-3})**	**92.5%**	**This Work**
MXene		**202.1 (1.0 A cm^{-3})**	**1.0-100 (A cm^{-3})**	**51.4%**	
$Ti_3C_2T_x$ MXene	1M $EMIMBF_4$/AN (-0.8-1.0 V) Three-electrode system	245 (2.0 mV s^{-1})	2.0-100 (mV s^{-1})	75%	28
$Ti_3C_2T_x$ MXene	$EMIMBF_4$ (0-3.0 V) Two-electrode system	140 (0.3 A cm^{-3})	0.3-3.0 (A cm^{-3})	52.8%	29
Other 2D material-based film electrodes					
BNP-HGH	$EMIMBF_4$/AN (0-3.5 V) Two-electrode system	234 (0.69 A cm^{-3})	0.69-69 (A cm^{-3})	57.7%	30
HGF	$EMIMBF_4$/AN (0-3.5 V) Two-electrode system	212 (0.71 A cm^{-3})	0.71-71 (A cm^{-3})	~67.8%	31
EM-CCG film	$EMIMBF_4$/AN (0-3.5 V) Two-electrode system	261.3 (0.125 A cm^{-3})	0.125-12.5 (A cm^{-3})	~37.9%	32
EGM-rGO film	$EMIMBF_4$ (0-3.0 V) Two-electrode	203 (0.94 A cm^{-3})	0.94-94 (A cm^{-3})	~73.9%	33

	system				
HGP	$EMIMBF_4$/AN (0-3.5 V) Two-electrode system	203 (1.12 A cm^{-3})	1.12-22.4 (A cm^{-3})	~68.9%	34
BNSs	PVDF-HFP/$EMIBF_4$ (0-3.0 V) Two-electrode system	310 (0.1 A cm^{-3})	0.1-10 (A cm^{-3})	~30.6%	35

Note: BNP-HGH: boron, nitrogen, and phosphorus ternary-doped holey graphene hydrogel, HGF: holey graphene framework, EM-CCG film, liquid electrolyte-mediated chemically converted grapheme, EGM-rGO film, exfoliated grapheme-mediated graphene oxide, HGP: holey graphene paper, B NSs: boron nanosheets.

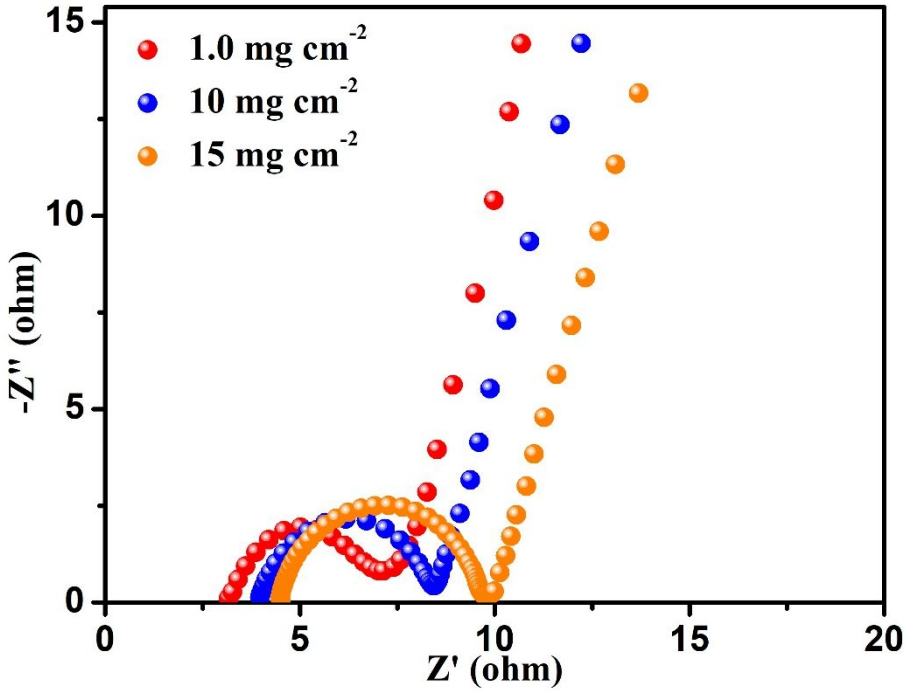

Figure S27. Nyquist plots of the BP@MXene-SCs (with BP@MXene mass loading of 1.0, 10 and 15 mg cm^{-2}).

Table S7. Fitting results for EIS of the three SCs.

Devices	R_s **(Ω)**	R_{ct} **(Ω)**	R_{ESR}	C_{DL}	W
BP@MXene-SC (1.0 mg cm^{-2})	3.21	3.87	7.14	0.75123	0.66325
BP@MXene-SC (10 mg cm^{-2})	3.96	4.45	8.41	0.76521	0.674125
BP@MXene-SC (15 mg cm^{-2})	4.52	5.31	9.83	0.697412	0.687569

References

(1) Liu, C.; Yan, X.; Hu, F.; Gao, G.; Wu, G.; Yang, X. Toward Superior Capacitive Energy Storage: Recent Advances in Pore Engineering for Dense Electrodes. *Adv. Mater.* **2018,** *30*, 1705713.

(2) El-Kady, M. F.; Strong, V.; Dubin, S.; Kaner, R. B. Laser Scribing of High-Performance and Flexible Graphene-Based Electrochemical Capacitors. *Science* **2012**, *335*, 1326–1330.

(3) Delley, B. An All-Electron Numerical Method for Solving the Local Density Functional for Polyatomic Molecules. *J Chem. Phys.* **1990**, *92,* 508.

(4) Pack, J. D.; Monkhorst, H. J.; Freeman, D. L. Lithium Crystal Properties from High-Quality Hartree-Fock Wave Functions. *Solid State Commun.* **1979**. *29,* 723–725.

(5) Hertwig, R. H.; Koch, W. On the Parameterization of the Local Correlation Functional. *Chem. Phys. Lett.* **1997,** *268,* 345–351.

(6) Monkhorst, H. J.; Pack, J. D. Special Points for Brillouin-Zone Integrations. *Phys. Rev. B* **1976**, *13,* 5188–5192.

(7) Chadi, D. J. "Special Points for Brillouin-Zone Integrations"–A Reply. *Phys. Rev. B* **1977**, *16,* 1746–1747.

(8) Ravel, B.; Newville, M. ATHENA, ARTEMIS, HEPHAESTUS: Data Analysis for X-Ray Absorption Spectroscopy Using IFEFFIT. *J Synchrotron. Radiat.* **2005,** *12,* 537–541.

(9) Koningsberger, D.; Prins, R. A Series of Monographs on Analytical Chemistry and Its Application. Wiley, **1988**, *92*.

(10) Rehr, J. J.; Albers, R. C. Theoretical Approaches to X-Ray Absorption Fine Structure. *Rev. Mod. Phys.* **2000**, *72,* 621–654.

(11) Yang, C.; Tang, Y.; Tian, Y.; Luo, Y.; He, Y.; Yin, X.; Que, W. Achieving of Flexible, Free-Standing, Ultracompact Delaminated Titanium Carbide Films for High Volumetric Performance and Heat-Resistant Symmetric Supercapacitors. *Adv. Funct. Mater*. **2018,** *28,* 1705487.

(12) Tian, Y.; Yang, C.; Que, W.; Liu, X.; Yin, X.; Kong, L. B. Flexible and Free-Standing 2D Titanium Carbide Film Decorated with Manganese Oxide Nanoparticles as a High Volumetric Capacity Electrode for Supercapacitor *J. Power Sources* **2017,** *359,* 332–339.

(13) Zhao, M. Q.; Ren, C. E.; Ling, Z.; Lukatskaya, M. R.; Zhang, C.; Van Aken, K. L.; Barsoum, M. W.; Gogotsi, Y. Flexible MXene/Carbon Nanotube Composite Paper with High Volumetric Capacitance. *Adv. Mater.* **2015,** *27*, 339–345.

(14) Yan, J.; Ren, C. E.; Maleski, K.; Hatter, C. B.; Anasori, B.; Urbankowski, P.; Sarycheva, A.; Gogotsi, Y. Flexible MXene/Graphene Films for Ultrafast Supercapacitors with Outstanding Volumetric Capacitance. Adv. Funct. Mater. **2017**, *27*, 1701264.

(15) Qin, L.; Tao, Q.; El Ghazaly, A.; Fernandez-Rodriguez, J.; Å. Persson, P. O.; Rosen, J.; Zhang, F. Polymer-MXene Composite Films Formed by MXene-Facilitated Electrochemical Polymerization for Flexible Solid-State Microsupercapacitors. *Adv. Funct. Mater.* **2018,** *28,* 1703808.

(16) Li, K.; Wang, X. H.; Li, S.; Urbankowski, P.; Li, J. M.; Xu, Y. X.; Gogotsi, Y. An Ultrafast Conducting Polymer@MXene Positive Electrode with High Volumetric Capacitance for Advanced Aasymmetric Supercapacitors. *Small* **2020,** *16,* 1906851.

(17) Lukatskaya, M. R.; Kota, S.; Lin, Z.; Zhao, M. Q.; Shpigel, N.; Levi, M. D.; Halim, J.; Taberna, P. L.; Barsoum, M. W.; Simon, P.; Gogotsi, Y. Ultra-High-Rate Pseudocapacitive Energy Storage in Two-Dimensional Transition Metal Carbides. Nat. Energy **2017**, *2*, 17105.

(18) Ghidiu, M.; Lukatskaya, M. R.; Zhao, M. Q.; Gogotsi, Y.; Barsoum, M. W. Conductive Two-Dimensional Titanium Carbide 'Clay' with High Volumetric Capacitance. *Nature* **2014**, *516,* 79–82.

(19) Fan, Z.; Wang, Y. S.; Xie, Z. M.; Wang, D. L.; Yuan, Y.; Kang, H. J.; Su, B. L.; Chen, Z. J.; Liu, Y. Y. Modified MXene/Holey Graphene Films for Advanced Supercapacitor Electrodes with Superior Energy Storage. *Adv. Sci*. **2018,** *5,* 1800750.

(20) Halim, J.; Kota, S.; Lukatskaya, M. R.; Naguib, M.; Zhao, M. Q.; Moon, E. J.; Pitock, J.; Nanda, J.; May, S. J.; Gogotsi, Y.; Barsoum, M. W. Synthesis and Characterization of 2D Molybdenum Carbide (MXene). Adv. Funct. Mater. **2016,** *26,* 3118–3127.

(21) VahidMohammadi, A.; Mojtabavi, M.; Caffrey, N. M.; Wanunu, M.; Beidaghi, M. Assembling 2D MXenes into Highly Stable Pseudocapacitive Electrodes with High Power and Energy Densities. *Adv. Mater.* **2019,** *31*, 1806931.

(22) Li, H. P.; Li, X. R.; Liang, J. J.; Chen, Y. S. Hydrous RuO_2-Decorated MXene Coordinating with Silver Nanowire Inks Enabling Fully Printed Micro-Supercapacitors with Extraordinary Volumetric Performance. *Adv. Energy Mater*. **2019,** *9,* 1803987.

(23) Yan, P.; Zhang, R.; Jia, J.; Wu, C.; Zhou, A.; Xu, J.; Zhang, X. Enhanced Supercapacitive Performance of Delaminated Two-Dimensional Titanium Carbide/Carbon Nanotube Composites in Alkaline Electrolyte. *J. Power Sources* **2015,** *284,* 38–43.

(24) Fu, Q.; Wang, X.; Zhang, N.; Wen, J.; Li, L.; Gao, H.; Zhang, X. Self-Assembled $Ti_3C_2T_x$/SCNT Composite Electrode with Improved Electrochemical Performance for Supercapacitor. *J. Colloid Interface Sci.* **2018,** *511,* 128–134.

(25) Wang, F.; Cao, M.; Qin, J.; Zhu, Y.; Wang, L.; Tang, Y. ZnO Nanoparticle-Decorated Two-Dimensional Titanium Carbide with Enhanced Supercapacitive Performance. *RSC Adv.* **2016,** *6,* 88934–88942.

(26) Lukatskaya, M. R.; Mashtalir, O.; Ren, C. E.; Dall'Agnese, Y. P.; Rozier, P. L.; Taberna, M.; Simon, P. M.; Barsoum, W.; Gogotsi, Y. Cation Intercalation and High Volumetric Capacitance of Two-Dimensional Titanium Carbide. *Science* **2013,** *341,* 1502–1505.

(27) Zheng, S.; Zhang, C.; Zhou, F.; Dong, Y.; Shi, X.; Nicolosi, V.; Wu, Z. S.; Bao, X. Ionic Liquid Pre-Intercalated MXene Films for Ionogel-Based Flexible Micro-Supercapacitors with High Volumetric Energy Density. *J. Mater. Chem. A* **2019,** *7*, 9478–9485.

(28) Tian, Y.; Yang, C.; Que, W.; Liu, X.; Yin, X.; Kong, L. B. Flexible and Free-Standing 2D Titanium Carbide Film Decorated with Manganese Oxide Nanoparticles as a High Volumetric Capacity Electrode for Supercapacitor. *J. Power Sources* **2017,** *359,* 332–339.

(29) Zhao, M. Q.; Ren, C. E.; Ling, Z.; Lukatskaya, M. R.; Zhang, C.; Van Aken, K. L.; Barsoum, M. W.; Gogotsi, Y. Flexible MXene/Carbon Nanotube Composite Paper with High Volumetric Capacitance. *Adv. Mater.* **2015,** *27*, 339–345.

(30) Pan, Z.; Zhi, H.; Qiu, Y.; Yang, J.; Xing, L.; Zhang, Q.; Ding, X.; Wang, X.; Xu, G.; Yuan, H.; Chen, M.; Li, W.; Yao, Y.; Motta, N.; Liu, M.; Zhang, Y. Achieving Commercial-Level Mass Loading in Ternary-Doped Holey Graphene Hydrogel Electrodes for Ultrahigh Energy Density Supercapacitors. *Nano Energy* **2018,** *46*, 266–276.

(31) Xu, Y.; Lin, Z.; Zhong, X.; Huang, X.; Weiss, N. O.; Huang, Y.; Duan, X. Holey Graphene Frameworks for Highly Efficient Capacitive Energy Storage. *Nat. Commun.* **2014,** *5*, 4554.

(32) Yang, X.; Cheng, C.; Wang, Y.; Qiu, L.; Li, D. Liquid-Mediated Dense Integration of Graphene Materials for Compact Capacitive Energy Storage. *Science* **2013,** *341*, 534–537.

(33) Li, Z.; Gadipelli, S.; Li, H.; Howard, C. A.; Brett, D. J. L.; Shearing, P. R.; Guo, Z.; Parkin, I. P.; Li, F. Tuning the Interlayer Spacing of Graphene Laminate Films for Efficient Pore Utilization towards Compact Capacitive Energy Storage. *Nat. Energy* **2020,** *5*, 160–168.

(34) Xu, Y.; Chen, C. Y.; Zhao, Z.; Lin, Z.; Lee, C.; Xu, X.; Wang, C.; Huang, Y.; Shakir, M. I.; Duan, X. Solution Processable Holey Graphene Oxide and Its Derived Macrostructures for High-Performance Supercapacitors. *Nano Lett.* **2015,** *15,* 4605–4610.

(35) Wu, T.; Wu, X.; Li, L.; Hao, M.; Wu, G.; Zhang, T.; Chen, S. Anisotropic Boron-Carbon Hetero-Nanosheets for Ultrahigh Energy Density Supercapacitors. *Angew. Chem. Int. Ed.* **2020,** *59,* 23800–23809.